JOURNAL OF MATERIALS SCIENCE 17 (1982) 3129–3139

Flaw growth in a polycrystalline lithium–aluminium–silicate glass ceramic

B. S. MAJUMDAR,* T. MAH, M. G. MENDIRATTA
Systems Research Laboratories Inc., 2800 Indian Ripple Road, Dayton, Ohio 45440, USA

The growth of indentation-produced "controlled" flaws in a polycrystalline lithium–aluminium–silicate glass ceramic has been studied, over a wide range of temperatures and strain rates. Significant scatter in the fracture stress at elevated temperatures suggests that the extent of slow crack growth is highly sensitive to microstructural details. The initial flaw shape is important in K_{IC} determination. Up to 1000° C the fracture toughness, K_{IC}, is essentially strain-rate insensitive. The value of K_{IC} decreases with temperature beyond 850° C. Intergranular cavity formation is suggested as the reason. Crack blunting by diffusive crack healing probably occurs at high temperatures. Also, intergranular slow crack growth occurs essentially under Mode I loading.

1. Introduction

Controlled-flaw growth experiments have recently been used to study the fracture behaviour of structural ceramics. The controlled flaws are produced by indenting the specimen surface with diamond indentions. These flaws are typically 100 μm, to simulate the growth of naturally occurring flaws.

The overall fracture process involves the following: (a) indentation cracking; (b) slow crack growth (only at high temperature); and (c) fast fracture. At present a few fairly good, although approximate, theoretical models on indentation crack have been developed [1–4]. Yet, as will be shown in this paper, certain aspects of indentation cracking require further development. Slow crack growth at high temperatures in polycrystalline ceramics is generally intergranular in nature. As shown by Lange [5], such intergranular fracture is not the corrosion-type phenomenon observed at room temperature in adverse environments. In time-to-failure and proof-stress calculations, it is generally assumed that the stress-intensity exponent, n, in the equation $v = AK^n$, is a material constant which is independent of local chemical and microstructural heterogeneities. This assumption warrants critical analysis. Finally, the temperature dependence of the stress-intensity factor at unstable fracture requires further study.

The present study was conducted on a model material, polycrystalline lithium–aluminum–silicate (LAS) glass ceramic, over a wide range of temperatures and loading rates. In addition, critical experiments were conducted in order to determine the effect of crack healing/blunting at high temperatures and also to investigate the effect of mixed-mode loading upon slow crack growth. All fracture tests were performed in four-point bending.

2. Experimental procedure

The LAS glass ceramic, purchased from Corning (no. 9617) was cut into bend bars approximately 50 mm long × 8 mm wide × 4 mm thick. The approximate composition (wt%) of the material (β-spodumene structure) is given in Table I.

The bars were ground on emery paper in order to remove any coating remaining from prior finishing treatments. The tension side of each bend bar was then carefully mechanically polished (up to 15 μm finish) using diamond paste. The cleaned samples were then annealed in air at 1100° C for 3 h. The

*Present address: Department of Mechanical Engineering, University of Rochester, Rochester, New York 14627, USA.

0022–2461/82/113129–11$03.82/0

TABLE I Composition of LAS glass ceramic

Compound	Li_2O	Al_2O_3	MgO	TiO_2	ZnO	ZrO_2	Fe_3O_4	CaO	Na_2O	SiO_2
Content (wt%)	3.5	21.4	2.3	4	1.9	0.24	0.29	0.14	0.27	65.96

bars were subjected to the annealing treatment in order to favorably modify the size and distribution of surface flaws. Experience with unannealed samples showed low strength and significant scatter in the fracture stress; the annealing treatment reduced the scatter considerably. After annealing, single indents were made at the centre of the tension side of the specimens, using a Vicker's diamond pyramid indentor. The indentor was oriented such that one set of radial cracks was aligned perpendicular to the maximum normal-stress direction. As a result these radial cracks behaved as Mode I flaws for subsequent fracture testing. Fig. 1 is a sketch of the geometry of the fracture samples. The indentor load was 2500 g, producing radial cracks $\sim 110\,\mu m$ in length. Fracture tests were also performed with Knoop indents, but the cracks produced were not always sharp and sufficiently deep and, as a result, final fracture did not always originate from the indents.

In some tests the indentor was oriented in such a way as to produce radial cracks at various angles to the principal normal-stress direction. These tests were carried out in order to evaluate crack propagation under a combination of Modes I, II, and III loading conditions and to determine whether intergranular slow crack growth occurs under mixed-mode loading.

Fracture testing was conducted in the Instron at temperatures ranging from room temperature to 1100° C, in air and in vacuum (10^{-4} Torr) environment. Testing was initiated 20 min after the desired temperature was reached. Cross-head speeds ranged from 0.005 to 1.25 cm min^{-1}, resulting in strain rates between $\simeq 3 \times 10^{-5}$ sec^{-1} and $\simeq 7 \times 10^{-3}$ sec^{-1} on the tension surface. The loading rate was varied in order to obtain different extents of slow crack growth. After fracture the fracture surfaces were coated with gold and observed in a Cambridge scanning electron microscope. The indented crack region and the zone of slow crack growth were easily discernible; therefore, K_{IC} could be determined from the crack size and load at fracture. Special features on the fracture surfaces were also noted.

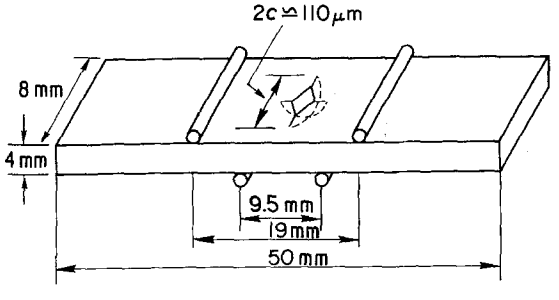

Figure 1 Schematic illustration of indented specimen and loading arrangement.

3. Results and discussion

3.1. Fracture stress

Fig. 2 shows the variation of fracture stress with cross-head speed at 1000° C. For all samples the indented radial cracks were oriented normal to the maximum principal stress direction. The data points correspond to tests conducted in 10^{-4} Torr vacuum. Results of tests conducted in air show no significant deviation from the vacuum data. Table II summarizes the test results. Fig. 3 is a schematic illustration of the fracture surface, showing regions of indented crack, slow crack growth, and fast fracture. The indented crack is nearly semicircular in shape. However, following slow crack growth, there is a change in shape of the crack front. The ratio a/c quantifies the ellipticity of the flaw at fast fracture. Table II shows a wide variation of a/c ratios. Nevertheless, there is always a general tendency for slow crack growth to occur along the length direction rather than along the depth, yielding a/c ratios less than unity.

Two other features in Fig. 2 are notable. The first is the significant scatter in the fracture stress, although fast fracture always originated at the indent. Similar scatter was observed in hot-pressed silicon nitride [6]. It is believed that such scatter is mainly caused by the irregular behaviour of slow crack growth, which results in variations of the flaw size and shape prior to fast fracture. However, in spite of the scatter, the fracture stress seems to increase monotonically with the strain rate. This behaviour may be contrasted with the results obtained by Govila *et al.* [7], where it was found that beyond a certain strain rate, the fracture stress decreased with an increase in strain rate.

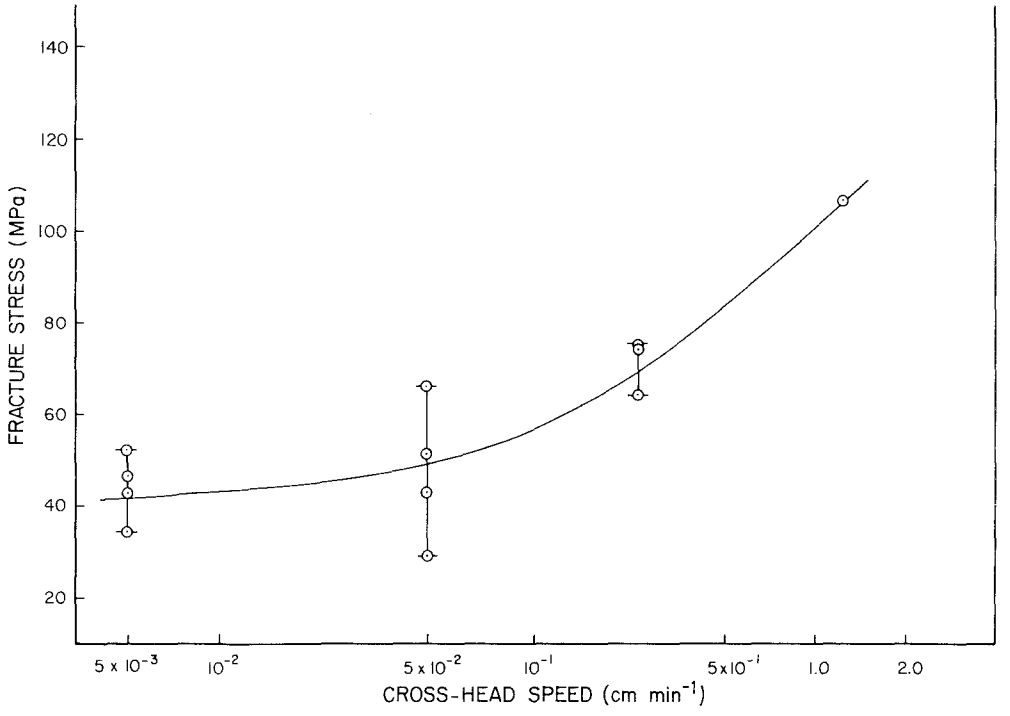

Figure 2 Variation of fracture stress with cross-head-speed at 1000° C in vacuum.

When the data in Fig. 2 are plotted on a log–log scale, in a manner normally employed in dynamic fatigue experiments, a stress-intensity exponent of ~ 6.5 is obtained. Here the stress-intensity exponent corresponds to n in the equation $\sigma_f = A\,\dot{\sigma}^{1/n+1}$ or $v = BK^n$, where $\dot{\sigma}$ is the stress rate, v the crack velocity, K the stress-intensity factor, σ_f the fracture stress, and A and B are constants. The value of n is quite reasonable. For example, in silicon nitride, n ranges from 8 to 12 [8, 9]. The other notable feature from Table II is the significant decrease in fracture stress from room

TABLE II

T(°C)	Rate (cm min^{-1})	Fracture stress, σ_f (MPa)	a/c	K_{IC} (MPa m$^{\frac{1}{2}}$)	Environment	Comments
25	0.005	135	1.057	1.39	air	
25	0.005	180	0.9	2.05	air	Indent was annealed in air at 1000° C for 3 h prior to fracture test
850	0.005	120	0.73	1.42	vacuum	
925	0.005	81	1.07	0.8	vacuum	
1000	0.005	52	0.78	0.52	vacuum	
1000	0.05	51	1.18	0.48	vacuum	
1000	0.05	62	1.12	0.62	air	
1000	0.25	64	0.97	0.63	vacuum	
1050	0.005	35	0.67	0.38	air	
1100	0.005	28	0.93	0.29	vacuum	
1100	0.005	24	0.71	0.24	air	
1100	0.05	41	0.40	0.76	vacuum	
1100	0.05	33	0.26	0.58	air	
1100	0.20	49	0.78	0.44	air	
1100	0.30	56	1.11	0.55	air	
1000	0.005	60			vacuum	Angular indent
1000	0.005	58			air	Angular indent

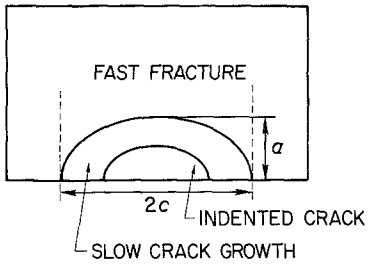

Figure 3 Schematic illustration of regions of indented crack, slow crack growth, and fast fracture. The flaw shape at fast fracture is approximated by a semi-ellipse of length $2c$ and depth a.

temperature (135 MPa) to 1000° C (52 MPa) at a cross-head speed of 0.005 cm min^{-1}. Further comments on this decrease will be made in a later section of this paper.

3.2. Fracture toughness

The fracture toughness, K_{IC}, can be calculated from the fracture stress, flaw size, and flaw shape at fast fracture. The critical flaw is taken to be the outer boundary of the slow crack growth regime. This boundary can always be delineated from the scanning electron micrographs. Fig. 4 is a micrograph of a fracture surface, showing well-defined regions A, B, and C which correspond to domains of the indented crack, slow crack growth, and fast fracture, respectively. Not always is the extent of slow crack growth so uniform in all directions as it is in Fig. 4. In any case, the final flaw shape was always approximated by a semi-ellipse, with the length of the flaw on the surface being set equal to $2c$, and the depth being set equal to a (see Fig. 3).

The value of K_{IC} was obtained at a point corresponding to the location of the maximum stress-intenisty factor, along the flaw boundary. The appropriate formula for K_{IC}, obtained from Bansal [10], was

$$K_{IC} = \frac{2\sigma_f\sqrt{a}}{Z}, \qquad (1)$$

where σ_f is the fracture stress, a the flaw depth, and Z a crack-shape parameter, i.e.

$$Z = E(k) \qquad \text{for } a \leqslant c$$

$$= \sqrt{\left(\frac{a}{c}\right)}\, E(k') \qquad \text{for } a \geqslant c.$$

$E(k)$ and $E(k')$ are the complete elliptic integrals of the second kind, with modulus $k = \sqrt{(1 - a^2/c^2)}$ and $k' = \sqrt{(1 - c^2/a^2)}$, respectively. Note that for $a/c \leqslant 1$, the maximum stress intensity occurs at a, and for $a/c \geqslant 1$ it occurs at the surface.

Using the formulae given above, K_{IC} was determined for various specimens. Fig. 5 shows the variation of K_{IC} with strain rate at 1000° C. Within the range of data available, K_{IC} is essentially a constant, equal to 0.5 MPa $m^{\frac{1}{2}}$. Of particular importance is the sharp decrease in scatter of the data, as compared to that in Fig. 2. For example, at a cross-head speed of 0.005 cm min^{-1}, the scatter in fracture stress is ± 25%, while the scatter in K_{IC} is only ± 5%. Such behaviour is expected if fracture toughness controls the strength of a member. The large variation in fracture stress is thus explained as being due to the scatter in the extent of slow crack growth. This variability in the domain of slow crack growth remains to be explained, although local variations in the microstructure and chemistry may be responsible in part.

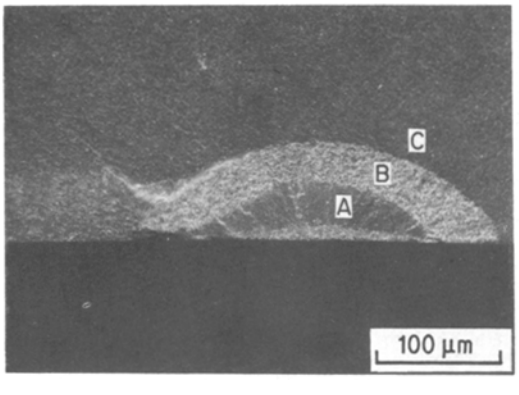

Figure 4 SEM of the fracture surface of a sample tested at 1000° C and 0.005 cm min^{-1}. A, indented crack; B, slow crack growth; C, fast fracture.

3.3. Temperature dependence of K_{IC}

Fig. 6 shows the temperature dependence of K_{IC}, at cross-head speeds of 0.005 and 0.05 cm min^{-1}. Data for tests conducted in both vacuum and air are included. Up to 850° C, K_{IC} remains essentially constant at 1.4 MPa $m^{\frac{1}{2}}$. Beyond that temperature K_{IC} decreases with temperature, reaching ~ 0.5 MPa $m^{\frac{1}{2}}$ at 1000° C. The behaviour is opposite to that observed in hot-pressed silicon nitride [7], where the fracture toughness was found to increase with temperature. However, K_{IC} dependence, similar to that presently observed, has been reported in hot-pressed silicon carbide [11].

At still higher temperatures, the value of K at

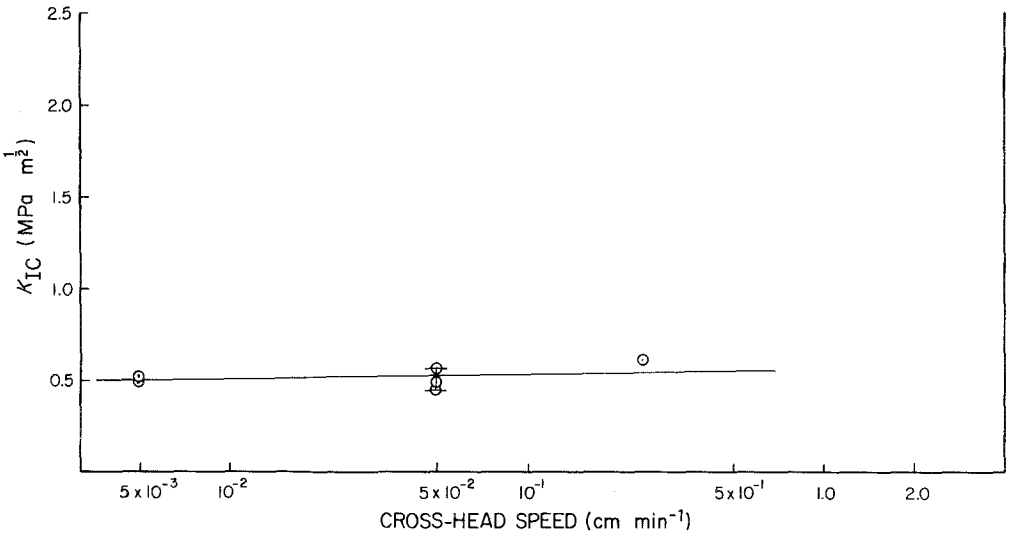

Figure 5 Variation of K_{IC} with cross-head speed at 1000° C.

instability depends quite sensitively upon strain rate. Thus, in vacuum at 1100° C, K_{IC} increases from 0.29 to 0.76 MPa $m^{\frac{1}{2}}$, for an increase in cross-head speed of 0.005 to 0.05 cm min^{-1}. In air the increase is from 0.24 to 0.58 MPa $m^{\frac{1}{2}}$, for the same range of cross-head speeds. It will be shown later that a significant fraction of intergranular damage occurs in the fast-fracture region at 1100° C. Such intergranular damage probably explains the strain-rate dependence of the fracture stress, since intergranular fracture is generally rate sensitive.

The curve in Fig. 6, which corresponds to a cross-head speed of 0.005 cm min^{-1}, shows that the effective surface energy γ ($\gamma = K^2/4E$, $E = 7.6 \times 10^4$ MPa) is $\sim 450 \times 10^{-7}$ J cm^{-2} at 1100° C. The surface energy of the grain-boundary liquid phase of the material under investigation is not known. However, a rough comparison may be made with liquid sodium silicate, whose surface energy is 250×10^{-7} J cm^{-2} at 1000° C [12]. Extrapolation of the curve in Fig. 6 shows that the surface energy of the present material would be 250×10^{-7} J cm^{-2} at 1170° C. Bearing in mind that the eutectic temperature of β-spodumene lies between 900 and 1000° C, and provided that crystallites do not melt, a temperature of 1200° C should be sufficient for complete intergranular fracture to occur at a cross-head speed of 0.005 cm min^{-1}.

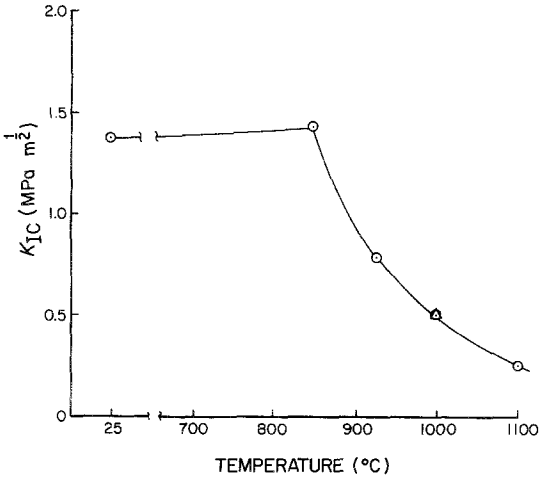

Figure 6 Variation of K_{IC} with temperature for specimens tested in vacuum. ⊙, 0.005 cm min^{-1}; △, 0.05 cm min^{-1} cross-head speed.

The decrease of K_{IC} with temperature needs some explanation. One possibility is the modulus effect, arrived at through the equation $K_{IC} = 2\sqrt{(E\gamma)}$. It is known that E is a very insensitive function of temperature. Therefore, the nearly three-fold decrease in K_{IC} from 850 to 1000° C cannot be explained by changes in E. The second possibility is based upon the premise that γ decreases with temperature. Note that γ is actually the free-energy increase of the solid per unit increase in surface area, at constant volume and temperature [13]. Thus,

$$\gamma = U_s - TS_s \qquad (2)$$

where U_s and S_s are, respectively, the energy and entropy change associated with formation of the

surface. Under the assumption that U_s and S_s are temperature independent,* one obtains

$$\gamma|_{T_2} - \gamma|_{T_1} = (T_1 - T_2)S_s. \quad (3)$$

The value of S_s is not known for the present material. However, for several metals it ranges from 0.5 to 3×10^{-7} J cm^{-2} K^{-1} [13]. Using the latter value for as only a rough estimate for S_s,

$$\gamma|_{1000°C} - \gamma|_{850°C} = 450 \times 10^{-7} \text{ J cm}^{-2}. \quad (4)$$

Using the data for K_{IC} and a modulus of 7.6×10^4 MPa, for the present material, one obtains

$$\gamma|_{1000°C} - \gamma|_{850°C} = 11\,200 \times 10^{-7} \text{ J cm}^{-2}. \quad (5)$$

This value is an order of magnitude higher than that predicted by Equation 4. Thus, the entropy effect is also unable to explain the temperature dependence of K_{IC}. It will be shown later that intergranular damage and cavity formation in the fast-fracture region offer an explanation for the temperature dependence of K_{IC}.

3.4. Fractography

Fig. 7 is a micrograph of the fracture surface of a sample tested at room temperature. Figs 8 and 9 are higher magnification micrographs in the indented-crack region and fast-fracture region, respectively. In both zones fracture is of the cleavage type. However, the distinct difference in morphology is worth noting. The fracture is directional and smooth in Fig. 8 and rough in Fig. 9. It is possible that the change in morphology occurs because of a difference in crack-growth rate in the two regimes. However, it is difficult to reconcile this possibility with the fact that a discontinuous change occurs in the fracture-surface morphology at the boundary between the indented-crack zone and the fast-fracture zone. If the morphology is simply velocity related, a transition zone should be observed in which the morphology changes gradually. The indentation process generates complex stress states involving an elasto-plastic deformation field. Therefore, the morphological differences may be associated with different stress states existing during indentation and fast fracture.

At temperatures of 1000° C and above, a distinct zone of slow crack growth is observed (Fig. 3). Fracture is intergranular in the slow-crack-

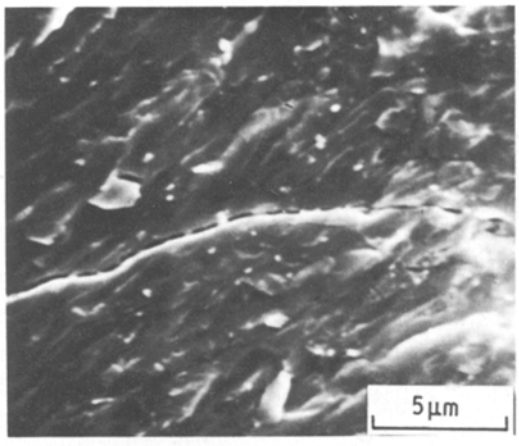

Figure 8 Higher magnification micrograph of indented crack region of Fig. 7. Note the flat mirror-like feature.

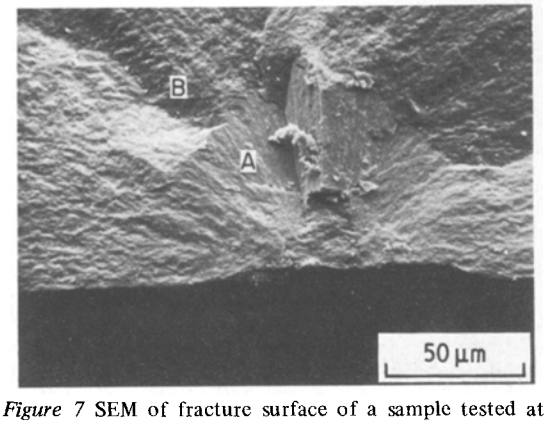

Figure 7 SEM of fracture surface of a sample tested at room temperature. A, indented crack; B, fast fracture. Note the discontinuous transition in fracture morphology at the boundary of Regions A and B.

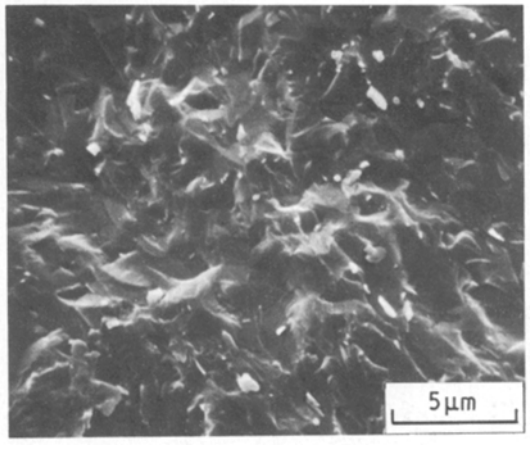

Figure 9 Higher magnification micrograph of fast-fracture region of Fig. 7. Note the characteristic transgranular cleavage fracture.

*Valid for several solid–liquid, solid–vapour interfaces of metals [13].

growth region, as shown in Fig. 10. At these high temperatures, a significant fraction of the grain boundaries is occupied by a liquid glassy phase. Since this phase would normally have lower surface energy than the interior of the grains, fracture should occur primarily along the grain boundaries. Such grain-boundary failure is thermally activated; therefore, the extent of slow crack growth would be cross-head-speed dependent which, in turn, would be manifested an an increase in fracture stress with strain rate, as shown in Fig. 2.

Closer observation of Fig. 10 shows a number of river lines, suggesting that transgranular cleavage fracture is present in addition to separation along the grain-boundary liquid phase. However, brittle failure along the remaining solid grain-boundary amorphous phase cannot be ruled out. Fig. 11 is a higher magnification micrograph of Fig. 10, showing relative rotation and separation along the grain boundaries. The process of intergranular fracture may, therefore, be summed up as follows: (a) formation of a liquid glassy phase along grain boundaries, (b) relative sliding and rotation between grains, giving rise to cavities, and (c) final separation between grains. It must be noted, however, that such intergranular fracture involves competition with a crack-healing process, especially because of the presence of the liquid glassy phase. In fact, there is indirect evidence that such a crack-healing process took place in the present material. This will be discussed in a later section of this paper.

Fig. 12 is a high-magnification micrograph showing regions immediately below the indentor (A), the indented crack (B), and the slow-crack-growth regime (C). The intergranular-type fracture immediately below the indentor should be noted. This feature was characteristic of most samples tested at high temperature. Such intergranular fracture is consistent with theories [3, 4] stating that during indentation, crack initiation occurs at a finite depth below the indentor, and not at the surface. The region immediately beneath the indentor may remain uncracked (or partially cracked); thus, the indented crack is really annular shaped rather than semicircular.

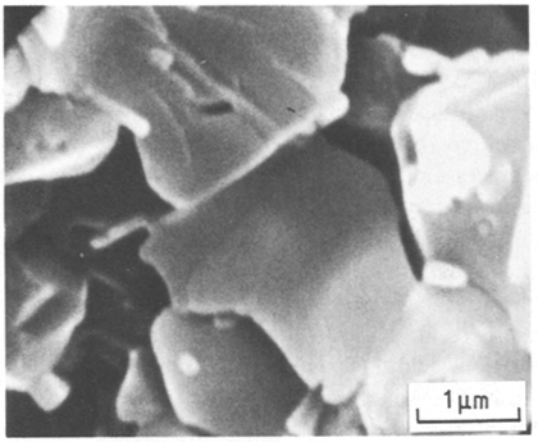

Figure 11 Higher magnification micrograph of the slow-crack-growth region of a specimen tested at 1000° C.

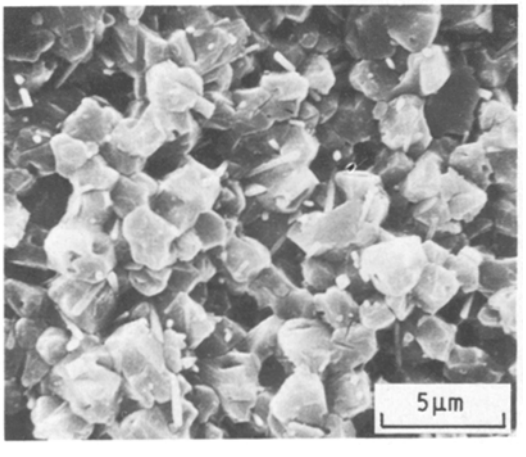

Figure 10 SEM of the slow-crack-growth region of a specimen tested at 1000° C at 0.005 cm min^{-1}. Fracture is intergranular.

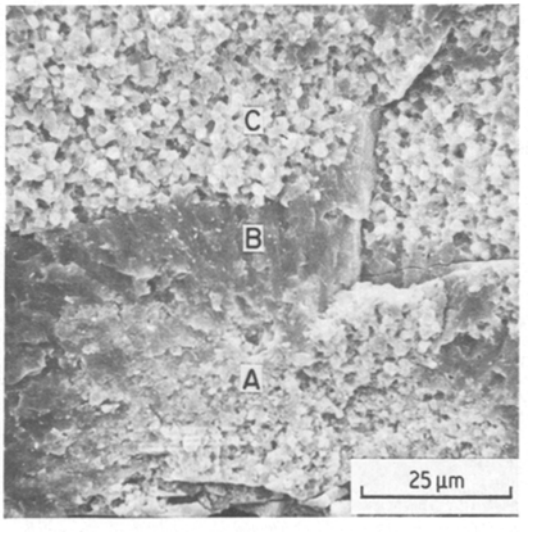

Figure 12 SEM of fracture surface of a specimen tested at 1100° C, showing regions immediately below the indentor (A), indented crack (B) and slow-crack-growth regime (C). The intergranular fracture immediately below the indentor should be noted.

Fig. 13 is an scanning electron micrograph in the fast-fracture region of a sample tested at 1000° C. Fracture is essentially of the cleavage type, although many of the cleavage steps are obscured by the glassy phase formed at the high temperature. In addition, a large number of cavities may be seen, having formed mainly at the triple points of the grain boundaries. It is very likely that the triple points have a higher concentration of the glassy phase. The nature of the microcracks suggests grain-boundary sliding and rotation. Sliding is a distinct possibility since at the high temperatures, the grain boundaries form liquid phases having fairly low surface energies ($\simeq 250 \times 10^{-7}$ J cm^{-2}). It is believed that nucleation of grain-boundary microcracks occurs in the stress field ahead of the main crack. Since plasticity within the grains is negligible even at high temperatures, the stress field can only be relaxed by relative sliding of the grain boundaries. Weaker bonding at the grain boundaries allows such phenomena. It is interesting to note that microcracks were not observed near the side surfaces of the samples. This observation suggests that a plane-strain tensile hydrostatic field is necessary for formation of cavities. This is consistent with the fact that for relative sliding of two surfaces to occur, a combination of shear and tensile stresses makes sliding easier as compared to the case where only shear stress is present. Also a tensile field would naturally aid the opening up of microcracks.

The formation of microcracks ahead of the main crack has important implications. Their presence would locally increase the stress-intensity factor of the main crack. Essentially this is a "crack-aiding" phenomena as opposed to the "shielding" of cracks when dislocations are emitted from crack tips [14]. The aiding of crack propagation by microcracks formed ahead of a main crack has also been mentioned by Evans and Wiederhorn [8] in their work on silicon nitride. Some calculations are given by Evans and Charles [15]. The calculations are rough and, therefore, no quantitative effect of microcracks has been assessed in this work. Nevertheless, the presence of microcracks in the fast-fracture region probably explains the sharp decrease in K_{IC} with temperature of 850° C and above.

At 850° C cavities are absent in the fast-fracture region. The fracture surface is similar to that observed at room temperature. Fig. 14 shows the fast-fracture region of a sample tested at 1100° C at 0.005 cm min^{-1}. The significant size and number of cavities is noteworthy. This micrograph should be compared with Fig. 13. Thus, as testing temperature is increased beyond 850° C, cavities begin to appear and their size increases gradually. These observations may be compounded with the K_{IC} data at 0.005 cm min^{-1} (Fig. 4), which show the fracture toughness to decrease from 1.4 to 0.29 MPa m$^{\frac{1}{2}}$ in the temperature range 850–1100° C. Fractographic analysis of a specimen tested in air at 1100° C at 0.2 cm min^{-1} showed fewer and smaller cavities, compared to those in Fig. 14. Here, also, the observation is consistent with the fact that K_{IC} was 0.4 MPa m$^{\frac{1}{2}}$ at 0.2 cm min^{-1}, compared to 0.24 MPa m$^{\frac{1}{2}}$ at 0.005 cm min^{-1}.

Fig. 15 shows the fast-fracture region in a specimen tested at 925° C. In this case the cavities

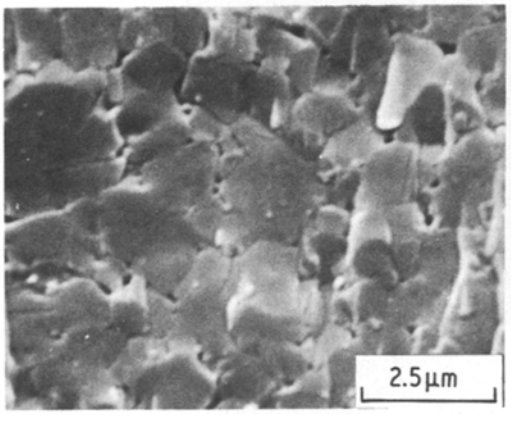

Figure 13 SEM of the fast-fracture region of a specimen tested at 1000° C.

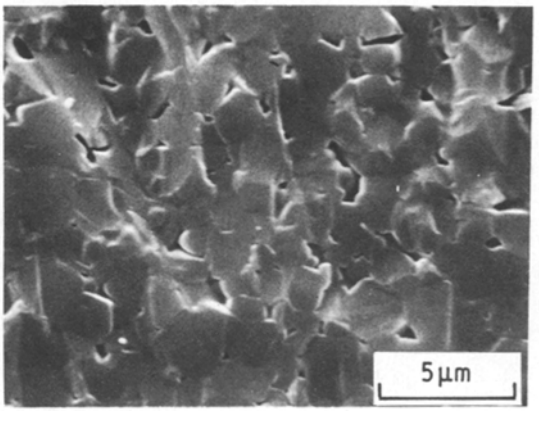

Figure 14 SEM of the fast-fracture region of a specimen tested at 1100° C. The size and number of cavities in this micrograph may be compared with those in Fig. 13.

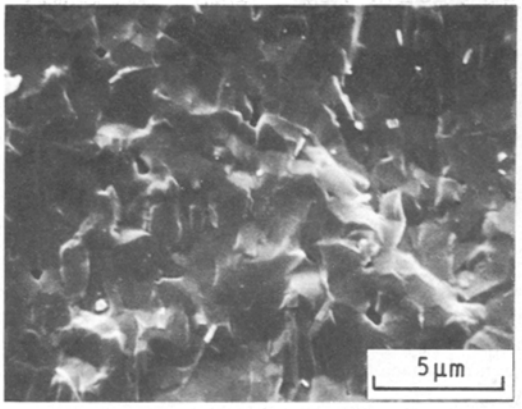

Figure 15 SEM of fast-fracture region of a specimen tested at 925° C. Note that the cavities are unevenly distributed.

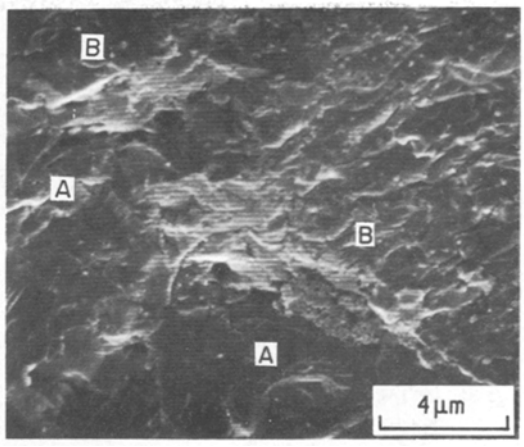

Figure 16 SEM of the fracture surface of a specimen near the boundary of the indented crack (A) and the fast fracture (B). Specimen was fractured at room temperature following annealing of the indent at 1000° C. The voids in the boundary region should be noted.

were unevenly distributed, with certain regions showing intergranular cavities and others showing no cavities at all. The intergranular damage is thus intermediate between 850 and 1000° C. A K_{IC} of 0.8 MPa $m^{\frac{1}{2}}$ at 925° C is, therefore, understandable. These micrographs suggest that a "mixture" theory of transgranular and intergranular damage might explain the observed K_{IC} dependence upon temperature. It should also be mentioned that a gradual transition takes place in the fracture-surface topography from 850 to 1100° C, the fast-fracture regions becoming progressively smoother or flatter. The behaviour of K_{IC} may also depend upon such transition in topography. However, cavities probably play a more dominant role in lowering K_{IC}.

3.5. Crack-blunting phenomenon

As previously mentioned, crack blunting by the viscous grain-boundary phase is a distinct possibility. To test this hypothesis, a specimen was indented at room temperature and then annealed in air at 1100° C for 3 h. Subsequent fracture testing at room temperature yielded a K_{IC} of 2 MPa $m^{\frac{1}{2}}$. This may be compared with a K_{IC} of 1.4 MPa $m^{\frac{1}{2}}$ for specimens tested at room temperature immediately following indentation. As expected, the fast-fracture region was similar for the two types of specimens. The increase in K_{IC} for the annealed sample can, therefore, be explained by rounding of the crack tip by flow of the viscous glassy phase and limited extent of crack healing. A healing phenomenon was also inferred from the observation that in the annealed sample, voids were present in the boundary region between the indented and fast-fracture domains (Fig. 16). These voids presumably were left behind during the healing process, as suggested by Evans and Charles [15]. The viscous glassy phase should be rich in lithium; therefore, the boundary region should show a larger concentration of this element, as compared to the remainder of the fracture surface. Unavailability of Auger equipment prevented further work in this area.

3.6. Inclined cracks

Limited tests were conducted at 1000° C with indented cracks inclined at an angle to the maximum principal stress direction. The purpose was to determine the crack path and also whether slow crack growth was occurring under mixed-mode conditions. Indented cracks were made at angles of 30° and 45° (Fig. 17).

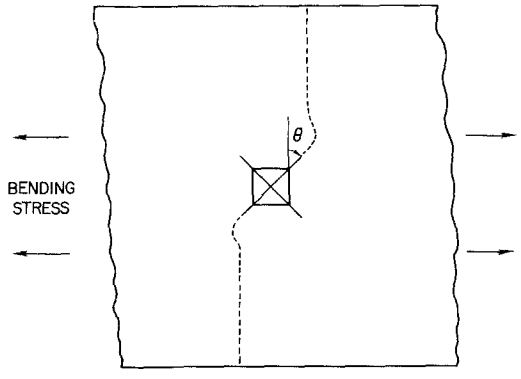

Figure 17 Schematic illustration of the fracture path for specimens with angular indent.

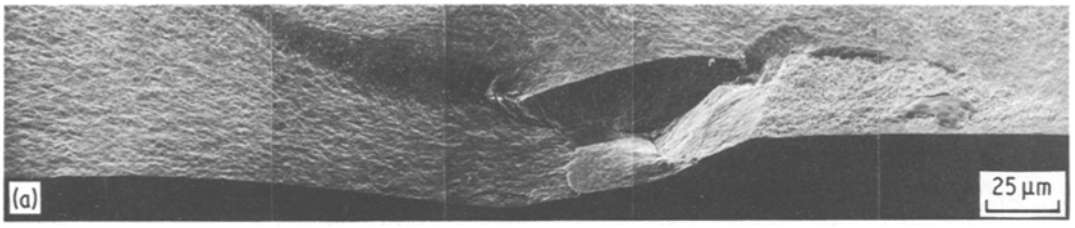

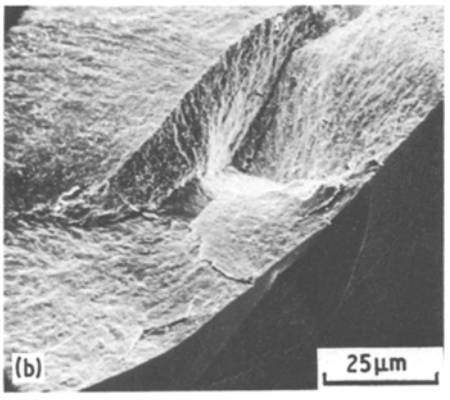

Figure 18 Two views of the fracture surface of a specimen with angular indent fractured at 1000° C. The specimen has been tilted in the microscope so that both the side surface (bottom of (a) and bottom right of (b)) and fracture surface (top of (a) and top left of (b)) are visible.

The dashed line in Fig. 17 shows, schematically, the general fracture path. Fracture tended to become normal to the bending-stress direction in all cases. In fact, when θ was 45°, fast fracture took place along the square edge of the indent. Presumably the median cracks terminate along the square edges of the indentor.

Fig. 18a and b shows two views of the crack path when $\theta = 30°$. In Fig. 18a the specimen has been tilted with respect to the electron beam, in such a way that both the side surface (bottom dark region) and fracture surface (top bright region) are visible. Fast fracture originated from the inclined indent; however, note (on the left side of the micrograph) that the crack gradually becomes orthogonal to the principal normal stress direction. Fig. 18b shows that fast fracture did not completely follow the indent. Here, too, is an indication that indented cracks are annular rather than semicircular.

The top right-hand side of Fig. 18a shows intergranular slow crack growth which occurs perpendicular to the principal bending-stress direction. Intergranular fracture did not occur on crack surfaces inclined at an angle to the bending-stress direction. These observations lead to the conclusion that slow crack growth occurs primarily under Mode I loading conditions.

4. Conclusions

(1) Fracture always occurs at the indent, indicating that the indentation crack may be used as a standard precrack for ceramics.

(2) At room temperature the indented fracture surface differs from the fast-fracture surface, and the morphology changes discontinuously in the boundary region. Mixed-mode cracking during indentation is suggested as a possible reason.

(3) Intergranular fracture (at high temperatures) in the region just below the indent verifies that cracking may not occur there during indentation.

(4) Large scatter in the fracture stress indicates that the extent of slow crack growth (also verified fractographically) is highly sensitive to microstructural and local chemical heterogeneities; this has important implications in proof-stress design.

(5) The initial flaw shape is important in K_{IC} determination.

(6) Over a wide temperature range, K_{IC} is independent of strain rate.

(7) K_{IC} decreases significantly with temperature beyond 850° C. Intergranular cavity formation is cited as the reason.

(8) Crack healing and blunting do occur at high temperatures.

(9) Intergranular slow crack growth occurs essentially under Mode I conditions, even when other modes are present.

Acknowledgement

The authors would like to thank Messrs Mark Rowe and George Cornish for conducting the mechanical testing. This work was supported under Contract F49620-77-C-0124 with the Air Force Office of Scientific Research.

References

1. D. B. MARSHALL and B. R. LAWN, *J. Mater. Sci.* **14** (1979) 2001.

2. D. B. MARSHALL, B. R. LAWN and P. CHANTIKUL, *ibid.* **14** (1979) 2225.
3. B. R. LAWN and A. G. EVANS, *ibid.* **12** (1977) 2195.
4. B. R. LAWN and M. V. SWAIN, *ibid.* **10** (1975) 113.
5. F. F. LANGE, *J. Amer. Ceram. Soc.* **57** (1974) 84.
6. M. G. MENDIRATTA and J. J. PETROVIC, *ibid.* **61** (1978) 226.
7. R. K. GOVILA, K. R. KINSMAN and P. BEARDMORE, *J. Mater. Sci.* **13** (1978) 2081.
8. A. G. EVANS and S. M. WIEDERHORN, *ibid.* **9** (1974) 270.
9. F. F. LANGE and J. L. ISKOE, "Proceedings of the Second Army Materials Technology Conference", Hyannis, Massachusetts 13–16 November, 1973), edited by J. J. Burke, A. E. Gorum and R. N. Katz (Brook Hill Publishing Co., Chestnut Hill, Mass, 1974) p. 223.
10. G. K. BANSAL, *J. Amer. Ceram. Soc.* **59** (1976) 87.
11. J. J. PETROVIC and L. A. JACOBSON, *ibid.* **59** (1976) 34.
12. W. D. KINGERY, "Introduction to Ceramics", (Wiley, New York, 1963).
13. R. A. SWALIN, "Thermodynamics of Solids" (Wiley, New York, 1972).
14. B. S. MAJUMDAR and S. J. BURNS, *Acta Met.* **29** (1981) 579.
15. A. G. EVANS and E. A. CHARLES, *ibid.* **25** (1977) 919.

Received 4 January
and accepted 15 March 1982